THE JOURNAL OF PHYSICAL CHEMISTRY Letters

Letter

Cite This: J. Phys. Chem. Lett. 2019, 10, 3153−3158

pubs.acs.org/JPCL

# Role of Valence Band States and Plasmonic Enhancement in Electron-Transfer-Induced Transformation of Nitrothiophenol

Robin Schürmann,[†,‡] Kenny Ebel,[†,‡] Christophe Nicolas,[§] Aleksandar R. Milosavljević,[§] and Ilko Bald*[,†,‡]

[†]Physical Chemistry, Institute of Chemistry, University of Potsdam, Karl-Liebknecht-Str. 24-25, 14476 Potsdam-Golm, Germany

[‡]Department of Analytical Chemistry BAM, Federal Institute of Material Research and Testing, Richard-Willstätter-Str. 11, 12489 Berlin, Germany

[§]Synchrotron SOLEIL, L'Orme des Merisiers, Saint Aubin, BP 48, 91192 Gif-sur-Yvette, France

Supporting Information

**ABSTRACT:** Hot-electron-induced reactions are more and more recognized as a critical and ubiquitous reaction in heterogeneous catalysis. However, the kinetics of these reactions is still poorly understood, which is also due to the complexity of plasmonic nanostructures. We determined the reaction rates of the hot-electron-mediated reaction of 4-nitrothiophenol (NTP) on gold nanoparticles (AuNPs) using fractal kinetics as a function of the laser wavelength and compared them with the plasmonic enhancement of the system. The reaction rates can be only partially explained by the plasmonic response of the NPs. Hence, synchrotron X-ray photoelectron spectroscopy (XPS) measurements of isolated NTP-capped AuNP clusters have been performed for the first time. In this way, it was possible to determine the work function and the accessible valence band states of the NP systems. The results show that besides the plasmonic enhancement, the reaction rates are strongly influenced by the local density of the available electronic states of the system.

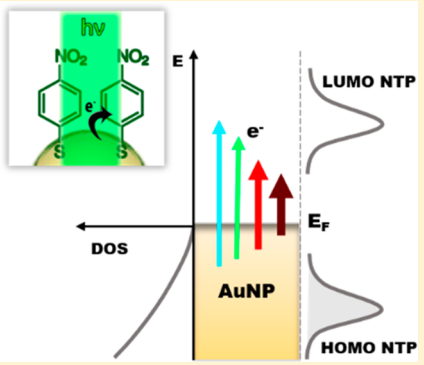


Localized surface plasmon resonances (LSPRs) strongly enhance the electric field in the vicinity of illuminated noble-metal nanoparticles (NPs), which enables versatile applications from sensing to catalysis.[1,2] In surface-enhanced Raman scattering (SERS), the increased near field in the vicinity of the NP surface is exploited to strongly enhance the inelastically scattered light of adsorbed molecules and consequently enhance the Raman signal by several orders of magnitude.[3,4] Moreover, chemical reactions of the adsorbed molecules can be mediated by the LSPRs.[5] One typical reaction mechanism is the transfer of a "hot electron", which is generated by the nonradiative decay of an LSPR.[2,6] Alternatively, a direct electron transfer from the hybridized states of the valence band of the NPs and the adsorbed molecules to the unoccupied molecular orbitals of the ligand molecules is likely.[2,7,8] In this case, the electron transfer crucially depends on the density of the available initial and final states.[9] The transformations from 4-aminothiophenol (ATP) or 4-nitrothiophenol (NTP), respectively, to 4-4-dimercaptoazobenzene (DMAB) are two of the most prominent plasmon-induced reactions studied widely with SERS and tip-enhanced Raman scattering and typically serve as model reactions.[10−12] Using SERS, the dimerization of NTP can be tracked;[13−15] however, the transformation to DMAB is rather complex, involving the transfer of four electrons per NTP molecule and several chemical equilibria.[16] Furthermore, the influence of thermal and electron-induced effects triggering the reaction has been controversially discussed.[17−19] Nevertheless, according to recent studies, a predominant role of the hot carriers in plasmonic catalysis is assumed.[20] Moreover, the metal band structure in plasmonic devices crucially determines the transport of hot carriers.[21] Within the present work, the influence of accessible valence band states on the reaction rates of the hot-electron-induced conversion of NTP is elucidated. Therefore, SERS is used as a method to monitor the plasmon-mediated reactions in real time.[22]

To fabricate a substrate for reproducible SERS measurements, a droplet of highly concentrated NTP-capped AuNPs (10 nm diameter) has been deposited on a freshly cleaned Si substrate. Besides the typical coffee-ring structures, relatively uniform areas of AuNPs have been formed during the drying process (see Figure 1a). Atomic force microscopy (AFM) images of these areas show flat AuNP multilayer structures with a quadratic surface roughness of ∼3 nm (see Figure 1b). In Figure 1c, a Raman image of the NTP signal at 1337 $cm^{-1}$ is presented, which is assigned to the $NO_2$ symmetric stretching vibration,[23] revealing very homogeneous and well-reproducible signal intensity with a standard deviation of ∼2% on these uniform areas.[24] In this way, for each SERS measurement,

Received: March 25, 2019
Accepted: May 21, 2019
Published: May 22, 2019






DOI: 10.1021/acs.jpclett.9b00848
J. Phys. Chem. Lett. 2019, 10, 3153−3158

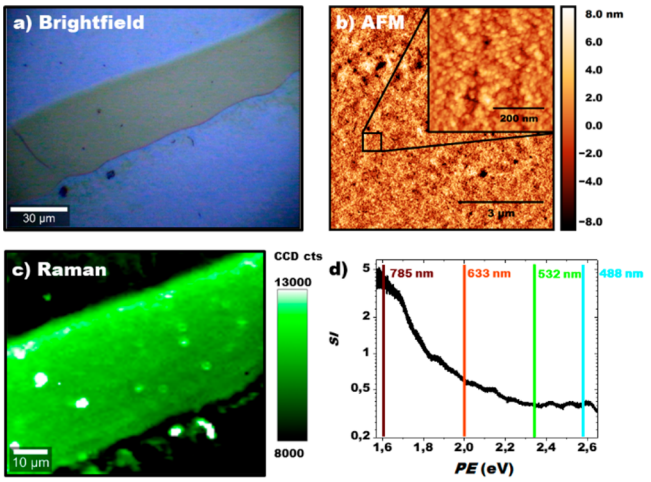


**Figure 1.** (a) Bright-field image of the AuNP substrate on a Si wafer. (b) AFM image of substrate with a size of 6 $\mu$m × 6 $\mu$m in the tapping mode. (c) Raman image with 100 × 100 pixels of the marked area recorded using a 633 nm laser with a power of 1 mW and focused with a 50× objective (NA = 0.75). Raman intensity of the 1337 $cm^{-1}$ signal is given as false colors. (d) Dark-field scattering intensity (SI) plotted as a function of the photon energy (PE). Colored bars mark the photon energies of the Raman lasers of the setup.

nonirradiated spots with almost identical reaction conditions can be addressed with the confocal microscope. The dark-field scattering spectrum (see Figure 1d) shows the characteristics of a plain gold surface with strong scattering in the red and near-infrared regions and a comparably low scattering in the blue and green regions of the visible light, which confirms the formation of homogeneous NP films.

In Figure 2a, time-dependent Raman measurements on the substrate are shown, which reveal a decrease in the Raman signals assigned to NTP with ongoing illumination time and an increase in new Raman bands assigned to the formation of DMAB

$$2\mathrm{NTP} + 8e^- \xrightarrow{+4H_2 - 4H_2O} \mathrm{DMAB} \quad (1)$$

The NTP $NO_2$ stretching vibration at the 1337 $cm^{-1}$ and 1445 $cm^{-1}$ bands of the $a_g$ modes of DMAB[25] have been used to track the reaction (see Figure 2b). On the basis of the ratio of these two signals, the observed reaction rate $k_{obs}$ after an illumination time $t$ can be determined (see the SI for details)

$$k_{obs} = \ln(1 + I_{1445\,cm^{-1}}/I_{1337cm^{-1}})/t \quad (2)$$

To rule out the influences of the desorption of the analytes and laser-induced modifications of the AuNP substrate, especially at high laser powers, it is important to determine the reaction rates using the ratio of the Raman bands. In Figure 2c, $k_{obs}$ is shown as a function of $t$, revealing a decrease following a power law. The time dependency of the reaction rate is caused by the inhomogeneous spatial distribution of the plasmonic enhancement on the nanoscale, as in the places with the highest field enhancement, the hot electrons are primarily generated;[26] consequently, plasmon-mediated reactions preferably take place in these hot spots.[27] The local reaction rate is given by

$$\text{local reaction rate} = k\cdot[\mathrm{NTP}]\cdot[e^-]^4 \quad (3)$$

where [NTP] is the concentration of NTP at a certain position on the plasmonic substrate, $[e^-]$ is the local hot electron generation rate, and $k$ is the reaction constant, which remains obscure when the reaction kinetics is studied with SERS. The generation rate of hot electrons is assumed to be time-independent, and thus the local reaction rate can be described by pseudo-first-order kinetics. Because the observed Raman signal is a summation over many hot spots, the observed reaction rate decreases with time, as the molecules that mainly contribute to the signal experience the highest rates. Previous kinetics studies of the dimerization of NTP[13,15] mainly did not take the influence of the inhomogeneity of the plasmonic enhancement into account, and hence the significance of the determined reaction constants and reaction orders is limited. van Schrojenstein Lantman et al. presented an approach to isolate the reaction taking place in the plasmonic hot spot from the bulk reaction of the molecules; however, a comparison of measurements under different reaction conditions is difficult with this method.[14] In the present study, the required time-independent reaction parameters, which allow at least a qualitative comparison of measurements under different reaction conditions, are obtained by applying fractal-like kinetics,[28] which has already been previously used to describe hot-electron-induced reactions.[29] The time-dependent reaction rate is given by

$$k_{obs} = k_1\cdot t^{-h} \quad (4)$$

where $k_1$ is the rate constant at a time $t$ = 1 s and $h$ is the fractal dimension of the system. The power law behavior of $k_{obs}$ most likely originates from the Pareto distribution of the plasmonic enhancement of coupled noble-metal NPs.[30] The reaction rates have been recorded at different laser wavelengths and powers, as shown in Figure 2d. Typically, the reaction rate should follow a power law where the exponent is given by the number of involved photons $N$[31]

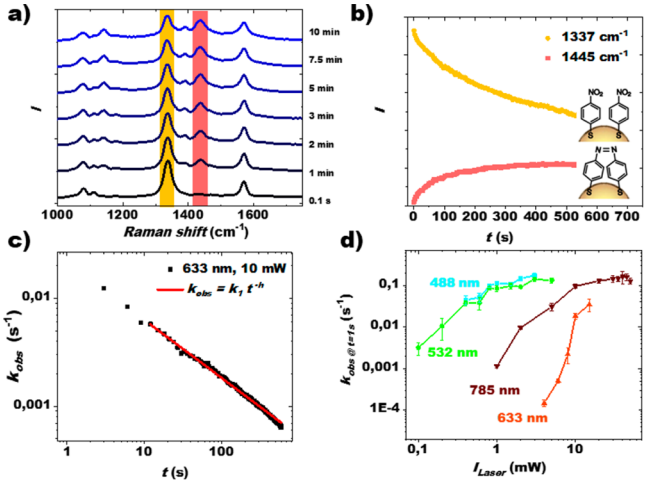


**Figure 2.** (a) Raman spectra of NTP on AuNPs recorded with a 633 nm laser and a laser power of 10 mW with 1 s of integration time after different illumination times. The yellow bar marks the $NO_2$ stretching vibration at 1337 $cm^{-1}$ of NTP, and the red bar marks the $a_g$ mode of DMAB at 1445 $cm^{-1}$. (b) Raman signal intensity of the two bands marked in panel a plotted as a function of the illumination time. (c) Observed reaction rates determined from eq 1 fitted with a power-law function. (d) Observed reaction rates at 1 s plotted as a function of the laser power for different laser wavelengths. Error bars are given from the standard deviation of three to five independent measurements.



DOI: 10.1021/acs.jpclett.9b00848
J. Phys. Chem. Lett. 2019, 10, 3153−3158

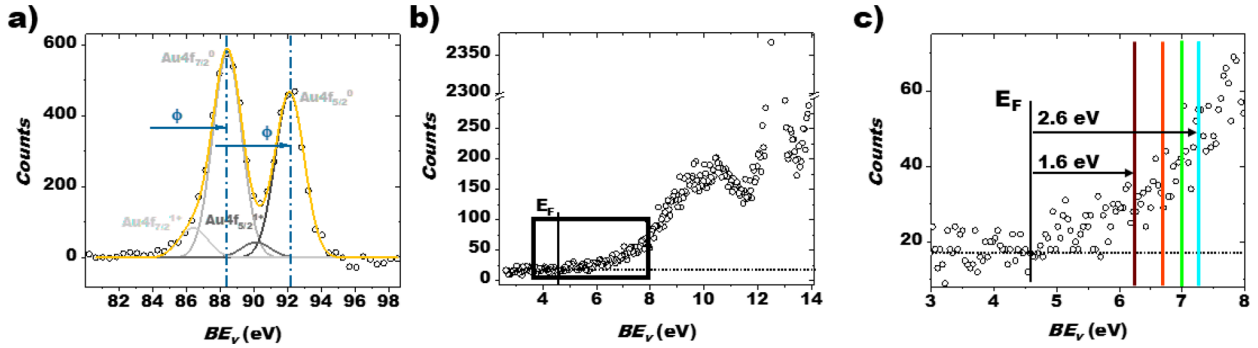


**Figure 3.** (a) Au 4f XPS spectra showing the 5/2 and 7/2 contributions of NTP-capped AuNPs recorded with a PE of 674.00 eV and a KE resolution of 1.9 eV. The spectrum is corrected by a Shirley-type background fitted with Gaussian curves. The blue arrows indicate the shift of the BE according to the work function. (b) Valence band states of the AuNP clusters recorded with a PE of 141.55 eV and a KE resolution of 0.2 eV. The signal at the $BE_v$ 12.6 eV from gas-phase water is used to validate the energy calibration of the KE of the photoelectrons. (c) Zoom-in of the valence band states. Colored lines mark the photon energies of the Raman laser with respect to $E_F$.

$$k_1 \propto I_{\text{laser}}{}^{N} \tag{5}$$

Because four electrons are involved in the transformation from NTP to DMAB (see eq 1), $N$ is expected to be 4. A value close to 4 has only been observed for the measurements using light with a wavelength of 633 nm ($N$ = 4.7 ± 0.8) for the investigated laser powers (fits presented in SI 2). For other excitation wavelengths, $N$ is clearly smaller than 4; however, because the reaction involves several chemical equilibria[16] and is influenced by thermal and nonthermal effects, the exact dependency on the laser power is supposed to be rather complex.[32] At higher laser powers, the increase in the reaction rate is less pronounced due to a trade-off with the thermally induced back reaction.[33] Overall, the highest reaction rates at a given laser power have been observed for illumination with 488 and 532 nm light, even though the plasmonic enhancement is comparably low in this wavelength region (Figure 1d). Nevertheless, for 785 nm laser light, where the plasmonic enhancement is the highest, the reaction rate is significantly higher than that for 633 nm light. Recent studies suggest that the reaction rates of hot-electron-induced reactions correlate with the dark-field scattering of the AuNP−substrate,[34] but the dependency of the reaction rates on the photon energy presented here can obviously not be explained solely by the plasmonic response of the substrate.

To monitor the electronic states of the AuNP/NTP system available for the electron-transfer-induced reaction, XPS measurements of isolated AuNPs clusters have been performed at the PLEIADES beamline of the synchrotron SOLEIL.[35−37] In the setup, a focused beam of NP clusters is crossed with a tunable soft X-ray beam under vacuum, and the kinetic energy (KE) of the generated photoelectron has been determined with an electron energy analyzer.[38] By using a beam of AuNPs in the gas phase instead of AuNPs deposited on a solid substrate, X-ray-induced damage of NTP is avoided.[39] Details of the experimental setup are presented in the SI. In brief, the NTP-capped AuNPs have been brought to the gas phase by an atomizer, and the size of the generated clusters prior to entering the ultra-high vacuum (UHV) chamber has been determined by differential mobility analysis, revealing a maximum of the size distribution at ∼150 nm (see SI 3).[38] The binding of the NTP on the AuNPs has been validated by the C 1s, N 1s, O 1s, and S 2p XPS spectra of the NP clusters (see SI 7). The absolute zero position and the linearity of the photoelectron KE scale have been calibrated according to the 3p, 3s, 2p, and 2s ionization potentials (IPs) of Ar[40,41] and the Ar $L_3M_{23}M_{23}$ Auger lines.[42] The photon energy (PE) has been calibrated by the Xe $3d_{5/2} \rightarrow 6p$ transition of Xe gas.[43] The overall uncertainty of the KE is estimated to be 0.2 eV. With the precisely determined PE and KE, the work function Φ of the NTP capped NPs can be determined by recording edges with a well-known binding energy (BE)

$$\Phi = \text{PE} - \text{BE} - \text{KE} \tag{6}$$

Because our NP beam is free-standing, all of the binding energies measured in the experiment are referenced to the vacuum level. Those binding energies will be noted with an index "$v$". To determine the work function of the NTP-capped AuNP clusters, the Au 4f spectra have been recorded using a photon energy of 674.00 eV to get a sufficiently high escape depth of the photoelectrons to pass the capping molecules (see Figure 3a). The Au $4f_{7/2}$ peak of the $Au^0$ was determined to be at a $BE_v$ of 88.4 ± 0.3 eV, which is shifted by (4.6 ± 0.5) eV according to the values previously reported, which were measured with respect to the Fermi level in the solid state.[44] (The uncertainty is given by the mean square root of the uncertainty of the $KE$, the fitting error, and the variation of values reported in the literature.) The difference of the BE is attributed to the work function of the AuNP clusters (see eq 5). Typically, the work function of AuNPs is ∼5.3 eV;[45] however, already due to the presence of a few layers of water, the work function can be shifted by 0.8 eV toward lower electron energies.[46] A similar decrease in the work function has been previously observed due to the adsorption of thiophenol derivates on copper surfaces.[47] We have determined the work function of citrate-capped AuNPs to be (4.2 ± 0.5) eV (see SI 8).

In addition to the core-level states of the NTP -capped AuNPs, the valence band states of the system have been recorded using a PE of 141.55 eV (see Figure 3b,c). With the knowledge of the work function, the recorded valence band states can also be discussed with respect to the Fermi level. The gaseous water state at $BE_v$ = 12.6 eV, which validates the energy calibration of the system, overlaps with a broad peak between 9 and 11 eV in $BE_v$, originating from the NP clusters (see SI 6). However, these states of the NP clusters are not accessible for electron transfers using visible light. Therefore, we focus on the onset of valence states, which is observed at the Fermi energy (highlighted in the box in Figure 3b). In the region between 0 and 2.6 eV, compared with the Fermi level,



DOI: 10.1021/acs.jpclett.9b00848
J. Phys. Chem. Lett. 2019, 10, 3153−3158

which is relevant for the light-mediated transformation of NTP to DMAB, the electron counts increase with higher BEs. The onset of the valence band structure is in accordance with previous studies of AuNPs with thiol-bound ligand molecules[48] and reflects the local density of occupied states in our system. The electron counts at 2.6 eV with respect to the Fermi level (indicated by the blue line in Figure 3c, corresponding to 488 nm excitation) are higher compared with those at 1.6 eV (indicated by the dark-red line in Figure 3c, corresponding to 785 nm excitation) by a factor of ∼3. The transition probability of an electron is proportional to the density of occupied states.[9] Because the transfer of four electrons for each NTP molecule is required for the conversion to DMAB, the increase in the density of occupied states leads to an increase in the transition probability by almost two orders of magnitude. Furthermore, the LUMO of NTP adsorbed on a gold surface is expected to be located 2 eV above $E_F$.[23] Hence, also the density of accessible unoccupied states increases when going from 785 to 488 nm excitation. An electron transfer into the low-energy onset of the LUMO is already possible at low photon energy (785 nm), but, in general, the transfer probability significantly increases with higher photon energies due to the higher density of both unoccupied molecular states and occupied NP states.

In Scheme 1, an energy diagram of the electronic initial and final states involved in the electron transfer from the AuNPs to the NTP molecules is sketched together with the photons of different wavelengths and plasmonic enhancements triggering the reaction. The higher density of accessible electronic states for photons with wavelengths of 488 (2.6 eV) and 532 nm (2.33 eV) compared with photons with longer wavelengths can qualitatively explain the high observed reaction rates, taking into account that four photons/electrons are involved in the process (see eq 5).

**Scheme 1. Schematic Energy Diagram of the Density of States (DOS) of the Valence Band of the AuNPs and the HOMO and LUMO of the Adsorbed NTP**[a]

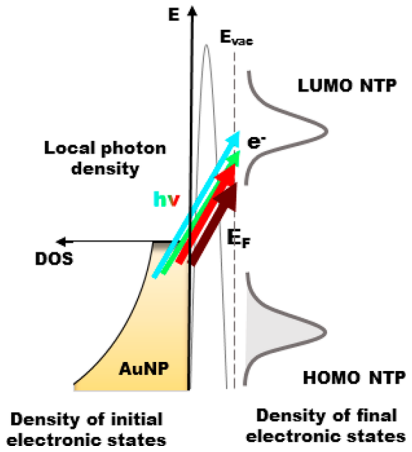


[a]Colored arrows represent the photons of the Raman lasers, and their width indicates the wavelength-dependent plasmonic enhancement.

A direct electron transfer is advantageous for the higher photon energies used here for the SERS measurements (see colored lines in Figure 3c); however, besides the electronic initial and final states, also the work function and the local density of photons[9] determine the electron-transfer probability. In consequence, the higher reaction rates using 785 nm compared with 633 nm laser light can most likely be explained by taking into account the strong plasmonic enhancement of the substrate in the near-infrared region, which increases the local photon density in this wavelength regime.

In summary, it is demonstrated that the dependency of the reaction rates of the plasmon-mediated transformation of NTP to DMAB on the excitation laser wavelength cannot be fully explained by the plasmonic response of the substrate. Moreover, the accessible electronic states of the NP−ligand system need to be considered to explain the reaction kinetics. Nevertheless, to derive a complete understanding of the kinetics in plasmon-catalyzed reactions in the future, further knowledge of the unoccupied state of the system and a real-time monitoring of all intermediate states are required. These findings will be crucial, on the one hand, to optimize plasmonic catalytic systems and, on the other hand, to find conditions for sensing applications, where the signal enhancement is high while unwanted electron-induced reactions are widely suppressed.

## ■ ASSOCIATED CONTENT

### Supporting Information

The Supporting Information is available free of charge on the ACS Publications website at DOI: 10.1021/acs.jpclett.9b00848.

Experimental section, XPS spectra from NTP ligands on AuNPs, XPS spectra from citrate ligands on AuNPs (PDF)

## ■ AUTHOR INFORMATION


### Corresponding Author

*E-mail: bald@uni-potsdam.de.

### ORCID

Aleksandar R. Milosavljević: 0000-0003-3541-8872

Ilko Bald: 0000-0002-6683-5065


### Notes

The authors declare no competing financial interest.

## ■ ACKNOWLEDGMENTS

This research is supported by the European Research Council (ERC; consolidator grant no. 772752). We acknowledge beamtime at the synchrotron SOLEIL through project 20171359. We thank Stephan Sass for his support in the synthesis of the AuNPs.

## ■ REFERENCES


(1) Zhan, C.; Chen, X.-J.; Yi, J.; Li, J.-F.; Wu, D.-Y.; Tian, Z.-Q. From plasmon-enhanced molecular spectroscopy to plasmon-mediated chemical reactions. *Nat. Rev. Chem.* **2018**, *2*, 216−230.

(2) Kim, Y.; Kazuma, E. Mechanistic studies of plasmon chemistry on metal catalysts. *Angew. Chem., Int. Ed.* **2019**, *58*, 4800−4808.

(3) Schlücker, S. Surface-enhanced Raman spectroscopy: Concepts and chemical applications. *Angew. Chem., Int. Ed.* **2014**, *53*, 4756−4795.

(4) Heck, C.; Kanehira, Y.; Kneipp, J.; Bald, I. Placement of Single Proteins within the SERS Hot Spots of Self-Assembled Silver Nanolenses. *Angew. Chem., Int. Ed.* **2018**, *57*, 7444−7447.

(5) Cortés, E. Activating plasmonic chemistry. *Science (Washington, DC, U. S.)* **2018**, *362*, 28−29.

(6) Zhang, Y.; He, S.; Guo, W.; Hu, Y.; Huang, J.; Mulcahy, J. R.; Wei, W. D. Surface-Plasmon-Driven Hot Electron Photochemistry. *Chem. Rev.* **2018**, *118* (6), 2927−2954.




DOI: 10.1021/acs.jpclett.9b00848
*J. Phys. Chem. Lett.* 2019, 10, 3153−3158

(7) Kale, M. J.; Avanesian, T.; Christopher, P. Direct Photocatalysis by Plasmonic Nanostructures. *ACS Catal.* **2014**, *4*, 116−128.
(8) Foerster, B.; Joplin, A.; Kaefer, K.; Celiksoy, S.; Link, S.; Sönnichsen, C. Chemical Interface Damping Depends on Electrons Reaching the Surface. *ACS Nano* **2017**, *11*, 2886−2893.
(9) Lindstrom, C. D.; Zhu, X.-Y. Photoinduced electron transfer at molecule-metal interfaces. *Chem. Rev.* **2006**, *106*, 4281−4300.
(10) van Schrojenstein Lantman, E. M.; Deckert-Gaudig, T.; Mank, A. J. G.; Deckert, V.; Weckhuysen, B. M. Catalytic processes monitored at the nanoscale with tip-enhanced Raman spectroscopy. *Nat. Nanotechnol.* **2012**, *7*, 583−586.
(11) Hartman, T.; Wondergem, C. S.; Kumar, N.; van den Berg, A.; Weckhuysen, B. M. Surface- and Tip-Enhanced Raman Spectroscopy in Catalysis. *J. Phys. Chem. Lett.* **2016**, *7*, 1570−1584.
(12) Kim, M.; Lin, M.; Son, J.; Xu, H.; Nam, J.-M. Hot-Electron-Mediated Photochemical Reactions: Principles, Recent Advances, and Challenges. *Adv. Opt. Mater.* **2017**, *5*, 1700004.
(13) Tang, X.; Cai, W.; Yang, L.; Liu, J. Monitoring plasmon-driven surface catalyzed reactions in situ using time-dependent surface-enhanced Raman spectroscopy on single particles of hierarchical peony-like silver microflowers. *Nanoscale* **2014**, *6*, 8612−8616.
(14) van Schrojenstein Lantman, E. M.; de Peinder, P.; Mank, A. J. G.; Weckhuysen, B. M. Separation of time-resolved phenomena in surface-enhanced Raman scattering of the photocatalytic reduction of p-nitrothiophenol. *ChemPhysChem* **2015**, *16*, 547−554.
(15) van Schrojenstein Lantman, E. M.; Gijzeman, O. L. J.; Mank, A. J. G.; Weckhuysen, B. M. Investigation of the Kinetics of a Surface Photocatalytic Reaction in Two Dimensions with Surface-enhanced Raman Scattering. *ChemCatChem* **2014**, *6*, 3342−3346.
(16) Choi, H.-K.; Park, W.-H.; Park, C.-G.; Shin, H.-H.; Lee, K. S.; Kim, Z. H. Metal-Catalyzed Chemical Reaction of Single Molecules Directly Probed by Vibrational Spectroscopy. *J. Am. Chem. Soc.* **2016**, *138*, 4673−4684.
(17) Golubev, A. A.; Khlebtsov, B. N.; Rodriguez, R. D.; Chen, Y.; Zahn, D. R. T. Plasmonic Heating Plays a Dominant Role in the Plasmon-Induced Photocatalytic Reduction of 4-Nitrobenzenethiol. *J. Phys. Chem. C* **2018**, *122*, 5657−5663.
(18) Keller, E. L.; Frontiera, R. R. Ultrafast Nanoscale Raman Thermometry Proves Heating Is Not a Primary Mechanism for Plasmon-Driven Photocatalysis. *ACS Nano* **2018**, *12*, 5848.
(19) Yu, Y.; Sundaresan, V.; Willets, K. A. Hot Carriers versus Thermal Effects: Resolving the Enhancement Mechanisms for Plasmon-Mediated Photoelectrochemical Reactions. *J. Phys. Chem. C* **2018**, *122*, 5040−5048.
(20) Zhou, L.; Swearer, D. F.; Zhang, C.; Robatjazi, H.; Zhao, H.; Henderson, L.; Dong, L.; Christopher, P.; Carter, E. A.; Nordlander, P.; Halas, N. J. Quantifying hot carrier and thermal contributions in plasmonic photocatalysis. *Science* **2018**, *362*, 69−72.
(21) Tagliabue, G.; Jermyn, A. S.; Sundararaman, R.; Welch, A. J.; DuChene, J. S.; Pala, R.; Davoyan, A. R.; Narang, P.; Atwater, H. A. Quantifying the role of surface plasmon excitation and hot carrier transport in plasmonic devices. *Nat. Commun.* **2018**, *9*, 3394.
(22) Xie, W.; Schlücker, S. Surface-enhanced Raman spectroscopic detection of molecular chemo- and plasmo-catalysis on noble metal nanoparticles. *Chem. Commun.* **2018**, *54*, 2326−2336.
(23) Zhao, L.-B.; Chen, J.-L.; Zhang, M.; Wu, D.-Y.; Tian, Z.-Q. Theoretical Study on Electroreduction of p-Nitrothiophenol on Silver and Gold Electrode Surfaces. *J. Phys. Chem. C* **2015**, *119*, 4949−4958.
(24) Kim, K.; Shin, D.; Kim, K. L.; Shin, K. S. Surface-enhanced Raman scattering of 4,4'-dimercaptoazobenzene trapped in Au nanogaps. *Phys. Chem. Chem. Phys.* **2012**, *14*, 4095−4100.
(25) Huang, Y.-F.; Zhu, H.-P.; Liu, G.-K.; Wu, D.-Y.; Ren, B.; Tian, Z.-Q. When the signal is not from the original molecule to be detected: Chemical transformation of para-aminothiophenol on Ag during the SERS measurement. *J. Am. Chem. Soc.* **2010**, *132*, 9244−9246.
(26) Manjavacas, A.; Liu, J. G.; Kulkarni, V.; Nordlander, P. Plasmon-induced hot carriers in metallic nanoparticles. *ACS Nano* **2014**, *8*, 7630−7638.
(27) Cortés, E.; Xie, W.; Cambiasso, J.; Jermyn, A. S.; Sundararaman, R.; Narang, P.; Schlücker, S.; Maier, S. A. Plasmonic hot electron transport drives nano-localized chemistry. *Nat. Commun.* **2017**, *8*, 14880.
(28) Kopelman, R. Fractal reaction kinetics. *Science (Washington, DC, U. S.)* **1988**, *241*, 1620−1626.
(29) Schürmann, R.; Bald, I. Real-time monitoring of plasmon induced dissociative electron transfer to the potential DNA radiosensitizer 8-bromoadenine. *Nanoscale* **2017**, *9*, 1951−1955.
(30) Le Ru, E. C.; Etchegoin, P. G.; Meyer, M. Enhancement factor distribution around a single surface-enhanced Raman scattering hot spot and its relation to single molecule detection. *J. Chem. Phys.* **2006**, *125*, 204701.
(31) Hla, S.-W. Scanning tunneling microscopy single atom/molecule manipulation and its application to nanoscience and technology. *J. Vac. Sci. Technol., B: Microelectron. Process. Phenom.* **2005**, *23*, 1351.
(32) Zhang, X.; Li, X.; Reish, M. E.; Zhang, Du; Su, N. Q.; Gutiérrez, Y.; Moreno, F.; Yang, W.; Everitt, H. O.; Liu, J. Plasmon-Enhanced Catalysis: Distinguishing Thermal and Nonthermal Effects. *Nano Lett.* **2018**, *18*, 1714−1723.
(33) Mahmoud, M. A. Reducing the photocatalysis induced by hot electrons of plasmonic nanoparticles due to tradeoff of photothermal heating. *Phys. Chem. Chem. Phys.* **2017**, *19*, 32016−32023.
(34) Dong, Y.; Jiang, P.; Xie, W. Harvesting hot electrons on Au nanoparticle monolayer by efficient compensation of holes. *Appl. Mater. Today* **2019**, *14*, 201−206.
(35) Meiling, T. T.; Schürmann, R.; Vogel, S.; Ebel, K.; Nicolas, C.; Milosavljević, A. R.; Bald, I. Photophysics and Chemistry of Nitrogen-Doped Carbon Nanodots with High Photoluminescence Quantum Yield. *J. Phys. Chem. C* **2018**, *122*, 10217−10230.
(36) Milosavljević, A. R.; Božanić, D. K.; Sadhu, S.; Vukmirović, N.; Dojčilović, R.; Sapkota, P.; Huang, W.; Bozek, J.; Nicolas, C.; Nahon, L.; Ptasinska, S. Electronic Properties of Free-Standing Surfactant-Capped Lead Halide Perovskite Nanocrystals Isolated in Vacuo. *J. Phys. Chem. Lett.* **2018**, *9*, 3604−3611.
(37) Sublemontier, O.; Nicolas, C.; Aureau, D.; Patanen, M.; Kintz, H.; Liu, X.; Gaveau, M.-A.; Le Garrec, J.-L.; Robert, E.; Barreda, F.-A.; Etcheberry, A.; Reynaud, C.; Mitchell, J. B.; Miron, C. X-ray Photoelectron Spectroscopy of Isolated Nanoparticles. *J. Phys. Chem. Lett.* **2014**, *5*, 3399−3403.
(38) Lindblad, A.; Söderström, J.; Nicolas, C.; Robert, E.; Miron, C. A multi purpose source chamber at the PLEIADES beamline at SOLEIL for spectroscopic studies of isolated species: Cold molecules, clusters, and nanoparticles. *Rev. Sci. Instrum.* **2013**, *84*, 113105.
(39) Roodenko, K.; Gensch, M.; Rappich, J.; Hinrichs, K.; Esser, N.; Hunger, R. Time-resolved synchrotron XPS monitoring of irradiation-induced nitrobenzene reduction for chemical lithography. *J. Phys. Chem. B* **2007**, *111*, 7541−7549.
(40) Thompson, A. C., Attwood, D. T., Gullikson, E. M., Howells, M. R., Kortright, J. B., Robinson, A. L., Underwood, J. H., Kim, K.-J., Kirz, J., Lindau, I., Pianetta, P., Winick, H., Williams, G. P., Scofield, J. H. *X-ray Data Booklet*; Lawrence Berkeley National Laboratory, University of California: Berkeley, CA, 2009.
(41) Svensson, S.; Eriksson, B.; Mårtensson, N.; Wendin, G.; Gelius, U. Electron shake-up and correlation satellites and continuum shake-off distributions in X-Ray photoelectron spectra of the rare gas atoms. *J. Electron Spectrosc. Relat. Phenom.* **1988**, *47*, 327−384.
(42) Werme, L. O.; Bergmark, T.; Siegbahn, K. The L2,3MM Auger Spectrum of Argon. *Phys. Scr.* **1973**, *8*, 149−153.
(43) Kato, M.; Morishita, Y.; Oura, M.; Yamaoka, H.; Tamenori, Y.; Okada, K.; Matsudo, T.; Gejo, T.; Suzuki, I. H.; Saito, N. Absolute photoionization cross sections with ultra-high energy resolution for Ar, Kr, Xe and N2 in inner-shell ionization regions. *J. Electron Spectrosc. Relat. Phenom.* **2007**, *160*, 39−48.
(44) Park, J.-W.; Shumaker-Parry, J. S. Structural study of citrate layers on gold nanoparticles: Role of intermolecular interactions in stabilizing nanoparticles. *J. Am. Chem. Soc.* **2014**, *136*, 1907−1921.


DOI: 10.1021/acs.jpclett.9b00848
*J. Phys. Chem. Lett.* 2019, 10, 3153−3158

(45) Carrara, M.; Kakkassery, J. J.; Abid, J.-P.; Fermín, D. J. Modulation of the work function in layer-by-layer assembly of metal nanoparticles and poly-L-lysine on modified Au surfaces. *ChemPhysChem* **2004**, *5*, 571−575.
(46) Musumeci, F.; Pollack, G. H. Influence of water on the work function of certain metals. *Chem. Phys. Lett.* **2012**, *536*, 65−67.
(47) Hong, S.-Y.; Yeh, P.-C.; Dadap, J. I.; Osgood, R. M. Interfacial dipole formation and surface-electron confinement in low-coverage self-assembled thiol layers: thiophenol and p-fluorothiophenol on Cu(111). *ACS Nano* **2012**, *6*, 10622−10631.
(48) Liu, H.; Mun, B. S.; Thornton, G.; Isaacs, S. R.; Shon, Y.-S.; Ogletree, D. F.; Salmeron, M. Electronic structure of ensembles of gold nanoparticles: Size and proximity effects. *Phys. Rev. B: Condens. Matter Mater. Phys.* **2005**, *72*, 1709.



DOI: 10.1021/acs.jpclett.9b00848
*J. Phys. Chem. Lett.* 2019, 10, 3153−3158